# Supporting Information

**Improving the Electrochemical Performance of Anionic Redox P3-Type Layered Oxide Cathode by the Synergistic Effect by Sodium Metaborate Coating and Boron Doping**

Zhenxiao Ling,[#a] Langyuan Wu,[#a] Yuxuan Xiang,[bc] Wendi Dong,[a] Lunjie Qin,[a] Xiaodong Qi,[a] Chaogen Hu[a] and Xiaogang Zhang*[a]

[a] Jiangsu Key Laboratory of Materials and Technologies for Energy Storage, College of Materials Science and Technology, Nanjing University of Aeronautics and Astronautics, Nanjing 210016, P. R.China.

[b] Research Center for Industries of the Future, Westlake University, Hangzhou, Zhejiang 310030, P. R. China.

[c] School of Engineering, Westlake University, Hangzhou, Zhejiang 310030, P. R. China.

* Corresponding Author E-mail: azhangxg@nuaa.edu.cn

[#] These authors contributed equally to this work.

**Experimental section**

**Materials Synthesis.**

P3-type $Na_{0.6}Li_{0.2}Mn_{0.8}O_2$ was synthesized using a solid-state reaction in which $Na_2CO_3$, LiOH, and $MnO_2$ were ball-milled in the acetone for four hours at 300 rpm, and 5 mol% $Na_2CO_3$ and 5 mol% LiOH were added to compensate for the heat loss. After drying in an oven at 80 °C, the precursors were pressed in an $Al_2O_3$ crucible and calcined at 670 °C in air for 24 hours.

The surface $NaBO_2$ coating and B doping P3-type NLMO cathode materials were prepared by the liquid-phase method and secondary annealing. $Na_2B_4O_7$-$10H_2O$, $Na_2CO_3$, and NLMO were dispersed in deionized water according to certain stoichiometric ratios and agitated at 80 °C until the deionized water was evaporated entirely, followed by the collection of the powder and secondary annealing. The secondary annealing process is completely consistent with the preparation of NLMO. The samples were named as 2%B-NLMO, 4%B-NLMO, 6%B-NLMO, and 8%B-NLMO according to the mass ratio of $NaBO_2$ generated by reaction Equation 1:

$$Na_2B_4O_7 + Na_2CO_3 \rightarrow 4NaBO_2 + CO_2 \tag{1}$$

To control the consistency of the experiments, the NLMO materials were treated with the same process and named as 0%B-NLMO. The calcined samples were transferred to a mortar, milled to powder, and kept in an argon-filled glove box.

**Electrochemical Measurements.**

The active material powder, polyvinylidene fluoride (PVDF) and acetylene black were evenly mixed in N-methyl-2-pyrrolidone (NMP) at a weight ratio of 8:1:1. The mixture was then applied to the carbon-coated aluminum foil and thereafter desiccated for a duration of 12 hours in a 110 °C vacuum oven. The electrodes were rolled and cut into 12 mm-diameter wafers with an active mass of 3-5 mg cm$^{-2}$. Using metal Na as the negative electrodes and porous glass fiber as the separators, coin cells (CR2032) were prepared in an argon-filled glove box for electrochemical measurements. The electrolyte was 1 M $NaPF_6$, and the mixed solvents were dimethyl carbonate (DMC), fluoroethylene carbonate (FEC), and propylene carbonate (PC) (DMC/FEC/PC=6:2:2 in mass). Galvanostatic charge and discharge (GCD) and galvanostatic intermittent titration technique (GITT) tests conducted using the Land test system.

Electrochemical impedance spectroscopy (EIS) was performed at the biological VMP-300 (EC-lab).

**Material Characterization.**

X-ray diffraction (XRD) tests were carried out using Empyrean (Malvern Panalytical) in the 2-theta range of 10°~80°. OPTIMA 8300 was utilized for inductively coupled plasma (ICP) test to evaluate the components of the samples. KRATOS AXIS SUPRA was used for X-ray photoelectron spectroscopy (XPS) testing. Fourier transform infrared (FTIR) spectra were measured on a Frontier IR/FIR STA 8000 spectrometer. Field emission scanning electron microscopy (FESEM, LYRA3 GMU) was used to confirm the particle morphology and conduct time-of-flight secondary ion mass spectrometry (TOF-SIMS) testing. High-resolution transmission electron microscopy (HRTEM, FEI Talos F200s) was utilized to observe the microstructure of the samples. The QMA410 system was used for differential electrochemical mass spectrometry (DEMS) test to monitor the gases produced from the cells during cycling. Solid-state $^7$Li nuclear magnetic resonance (NMR) measurements were performed with a 600-MHz Bruker Advance III spectrometer with a $^7$Li Larmor frequency of 233.34 MHz in a 14.1 T magnetic field.
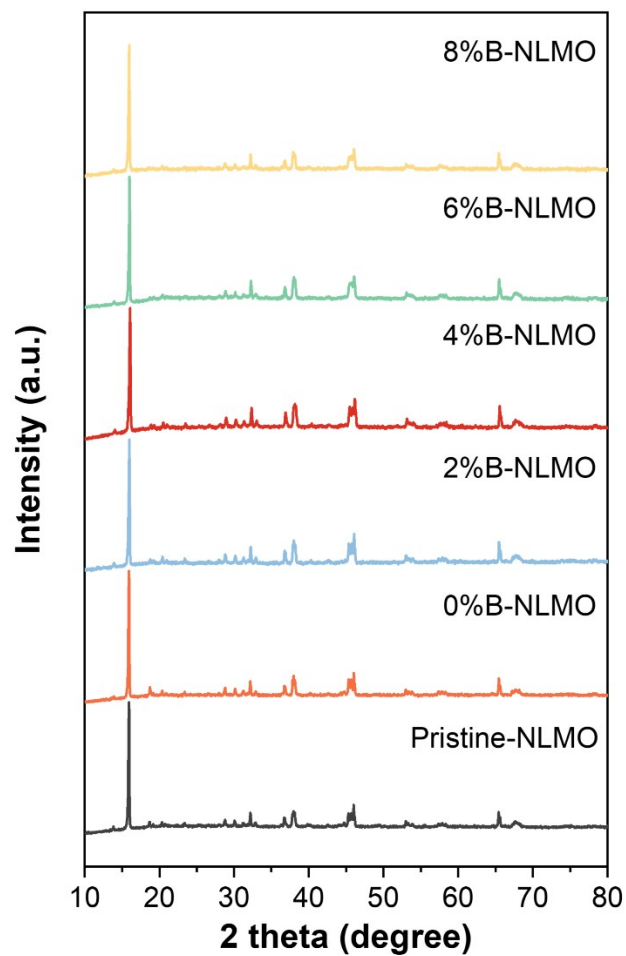
**Figure S1.** Powder XRD pattern of pristine-NLMO, 0%B-NLMO, 2%B-NLMO, 4%B-NLMO, 6%B-NLMO and 8%B-NLMO.
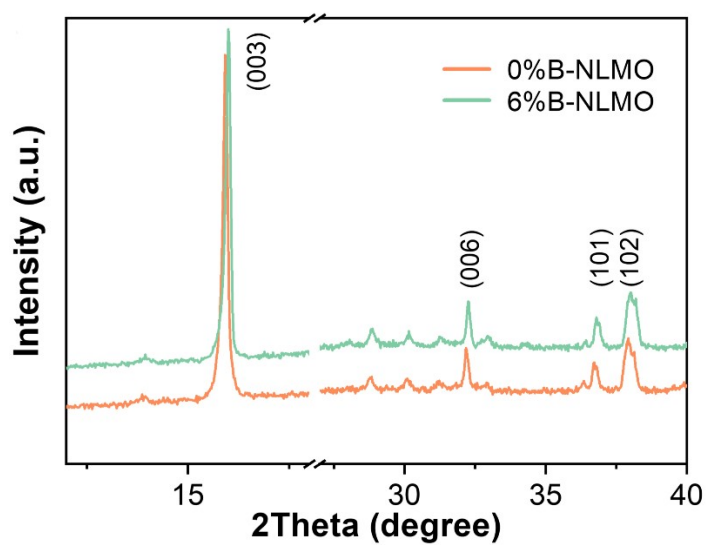


**Figure S2.** Powder XRD pattern of 0%B-NLMO and 6%B-NLMO.
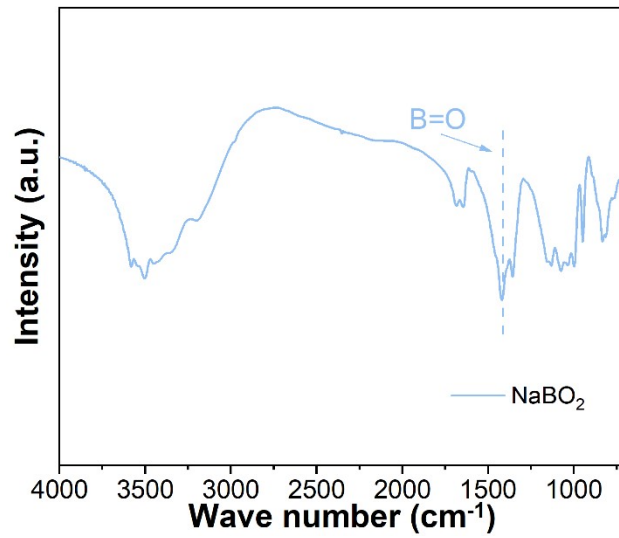
**Figure S3.** The FTIR spectra of $NaBO_2$.
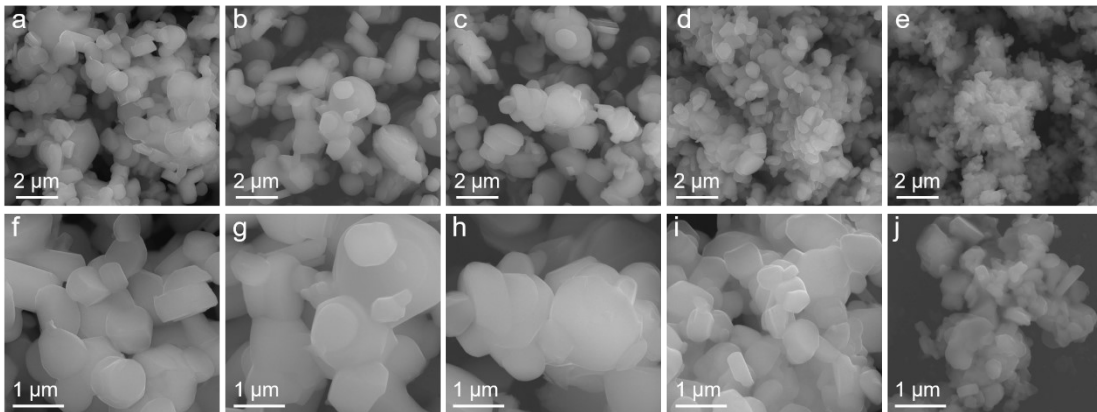


**Figure S4.** SEM images of (a,f) 0%B-NLMO, (b,g) 2%B-NLMO, (c,h) 4%B-NLMO, (d,i) 6%B-NLMO and (e,j) 8%B-NLMO.
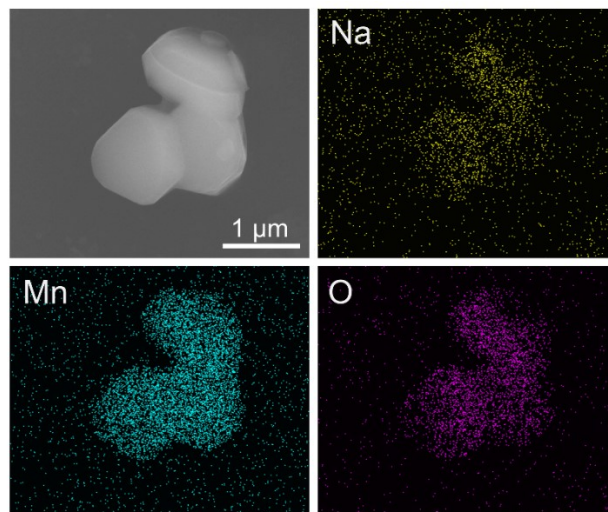


**Figure S5.** SEM images and EDX mapping of elements of 0%B-NLMO.
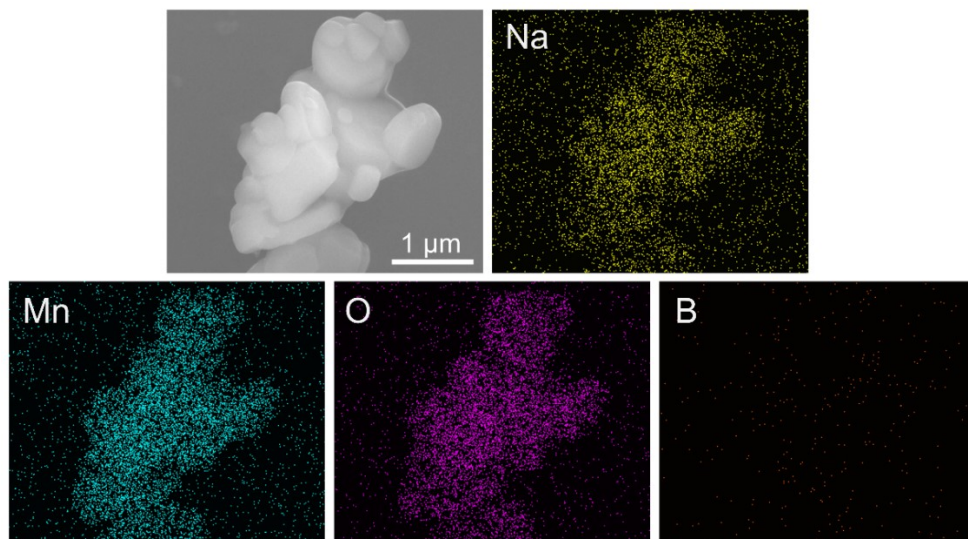
**Figure S6.** SEM images and EDX mapping of elements of 6%B-NLMO.
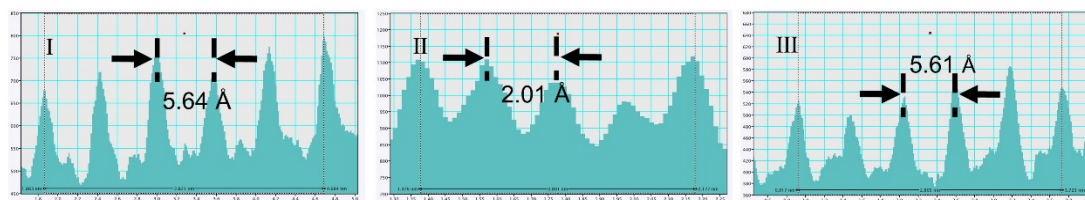


**Figure S7.** The corresponding lattice spacing for I, II, III regions in Fig. 5h and i.
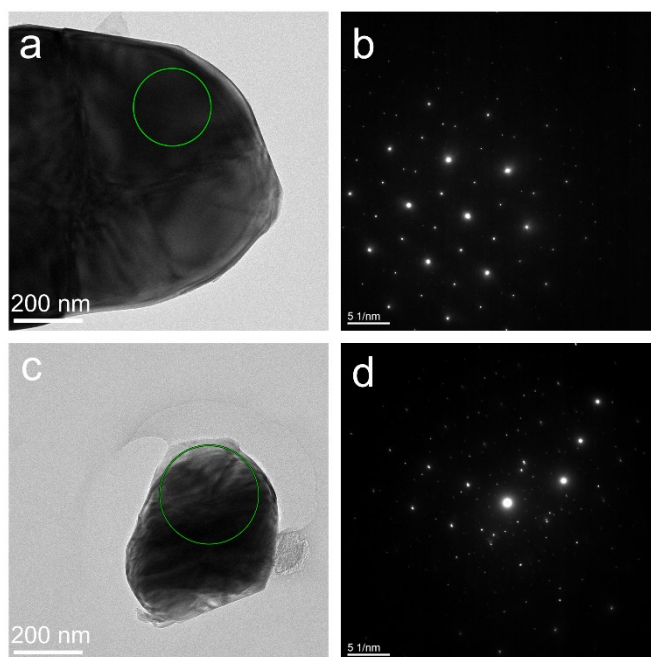


**Figure S8.** HRTEM images and corresponding selected-area electron diffraction of (a,b) 0%B-NLMO and (c,d) 6%B-NLMO
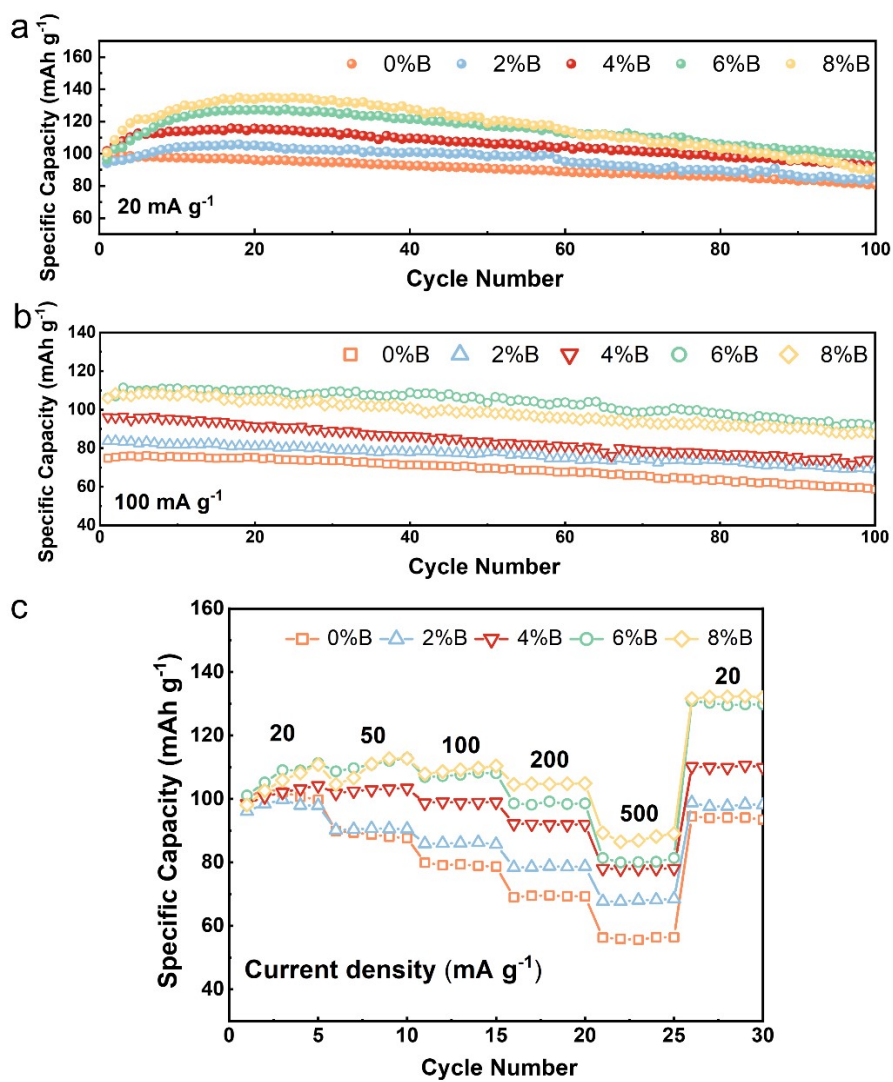
**Figure S9.** Cycling performances of 0%B-NLMO, 2%B-NLMO, 4%B-NLMO, 6%B-NLMO and 8%B-NLMO over 100 cycles at (a) 20 and (b) 100 mA g$^{-1}$. (c) Rate performance of 0%B-NLMO, 2%B-NLMO, 4%B-NLMO, 6%B-NLMO and 8%B-NLMO.
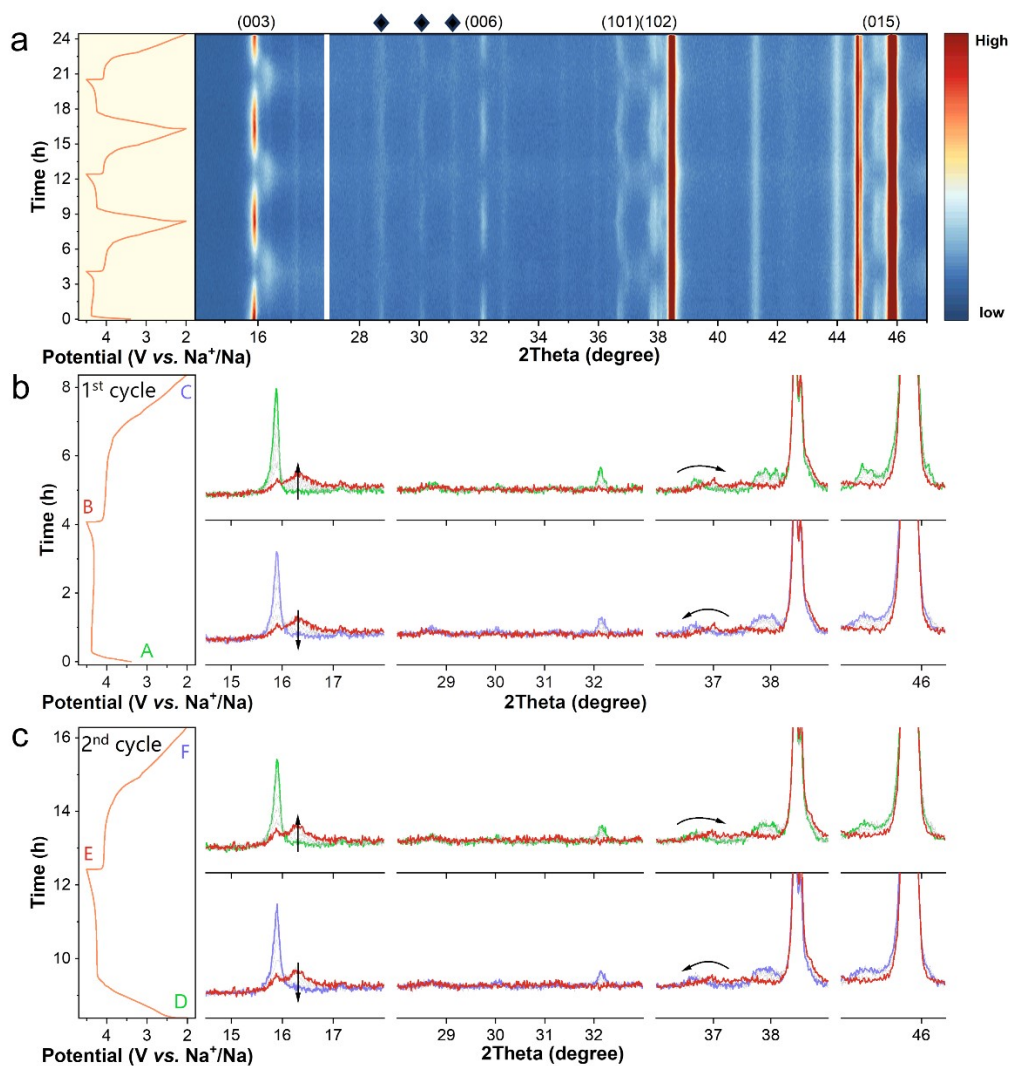
**Figure S10.** (a) In situ XRD contours plots and relative GCD curves of 0%B-NLMO during the first three cycles. The black diamond icons indicate the diffraction peaks of the ribbon-ordered superstructure. In situ XRD patterns and relative GCD curves of 0%B-NLMO during the (b) first and (c) second cycles. Points A, B, and C on the GCD curves represent the initial, fully charged, and fully discharged states in the first cycle, while points D, E, and F represent the initial, fully charged, and fully discharged states in the second cycle. These points correspond to the XRD curves of the same color on the right side.
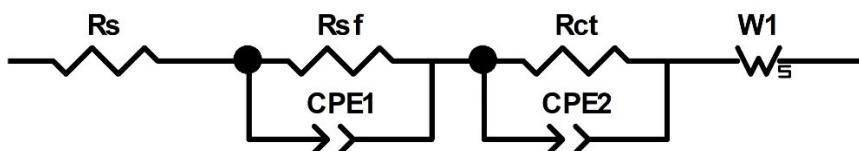


**Figure S11.** The corresponding equivalent circuit model for Nyquist plots.
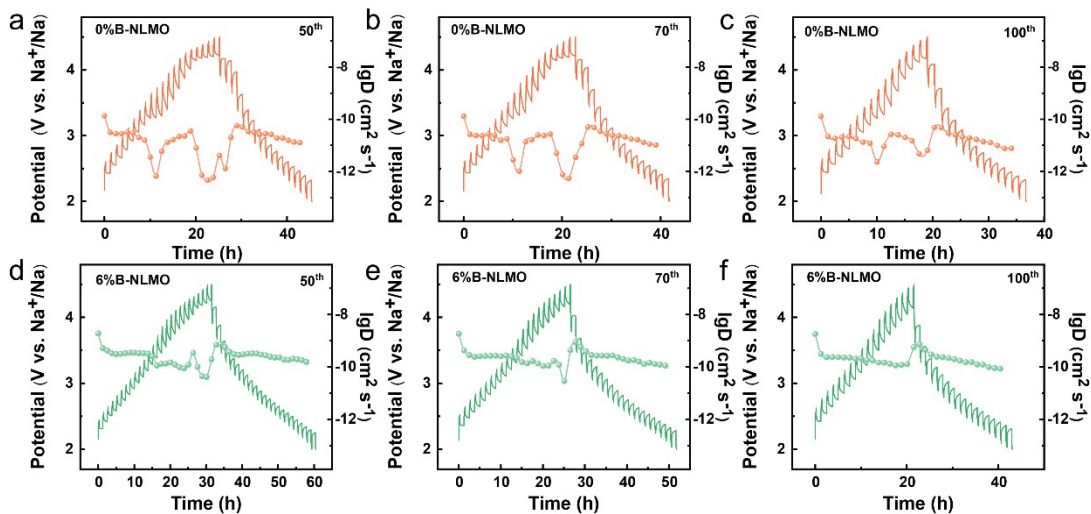
**Figure S12.** GITT curves and Na⁺ diffusion coefficient of (a-c) 0%B-NLMO and (d-f) 6%B-NLMO during the 50th, 70th, and 100th cycles.
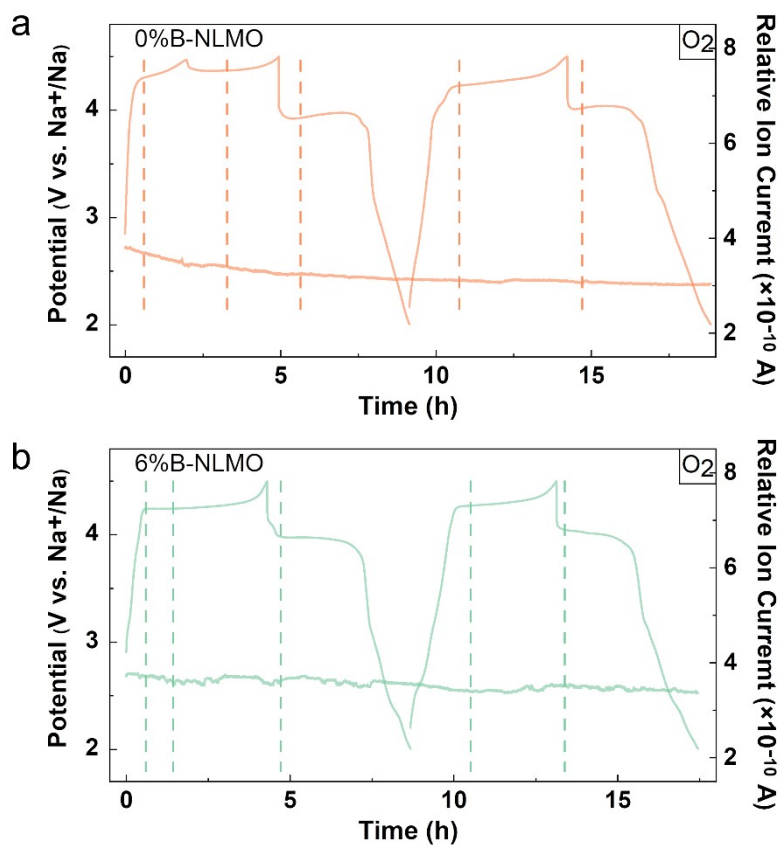


**Figure S13.** DEMS results of gas evolution for $O_2$ of (a) 0%B-NLMO and (b) 6%B-NLMO during the first two cycle.
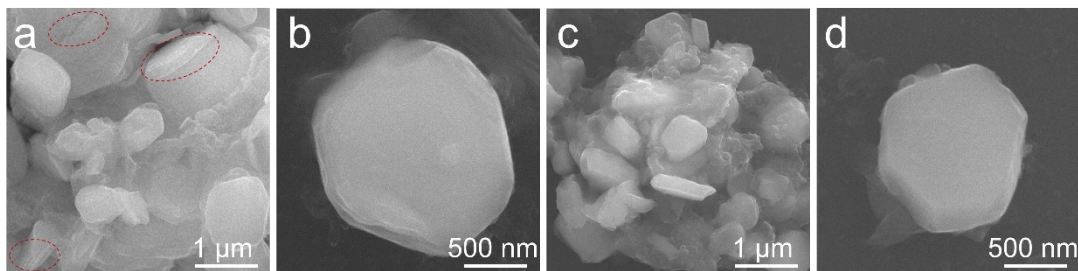
**Figure S14.** The SEM images of (a,b) 0%B-NLMO and (c,d) 6%B-NLMO particles after 100 cycles.
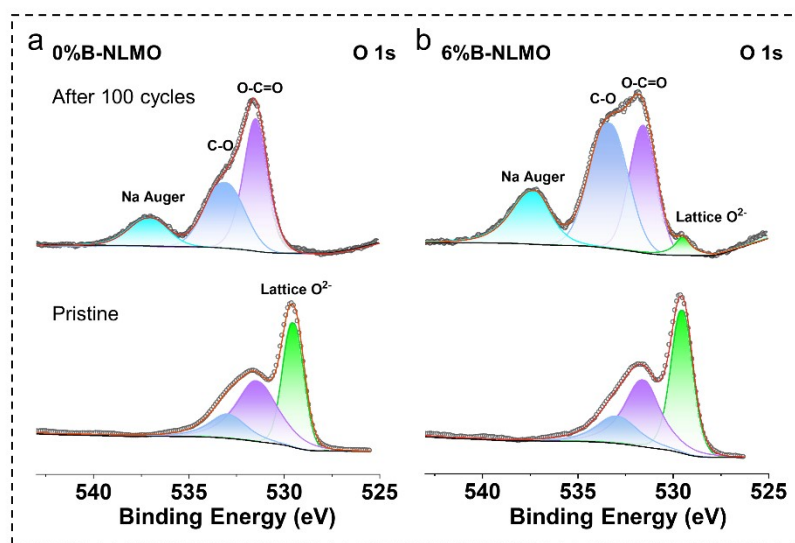


**Figure S15.** The O 1s XPS spectra of pristine and after 100 cycles of (a) 0%B-NLMO and (b) 6%B-NLMO.
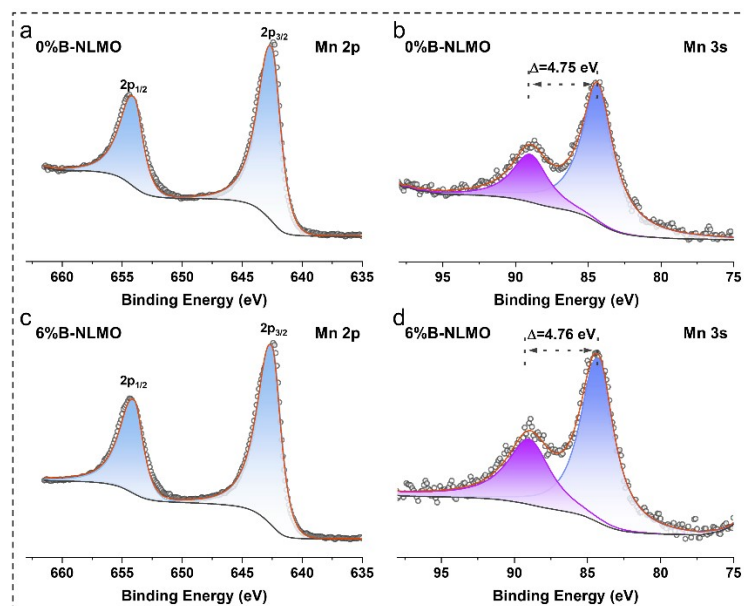


**Figure S16.** The (a) Mn 2p and (b) Mn 3s XPS spectra of pristine 0%B-NLMO. The (c) Mn 2p and (d) Mn 3s XPS spectra of pristine 6%B-NLMO.
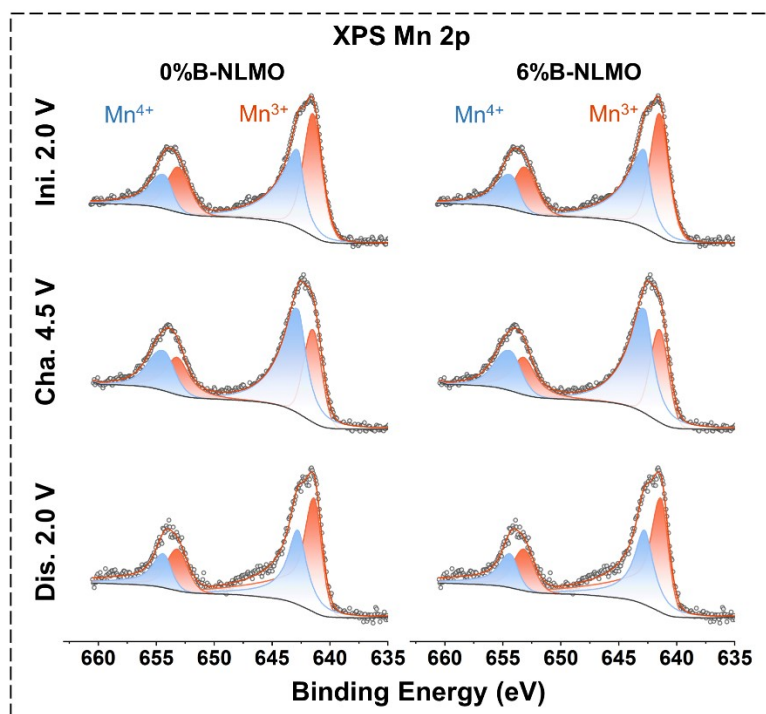
**Figure S17.** The Mn 2p XPS spectra of 0%B-NLMO and 6%B-NLMO at the initial, fully charged, and fully discharged states of the 10th cycle, respectively.
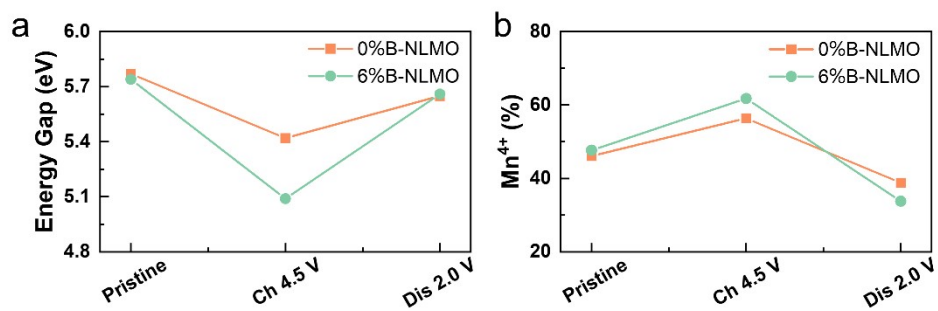


**Figure S18.** (a) Energy gap of Mn 3s spectra and (b) $Mn^{4+}$ content of 0%B-NLMO and 6%B-NLMO electrodes obtained according to XPS fitting results.